Journal of Materials Chemistry A

Targeted synthesis and reaction mechanism discussion of Mo2C based insertion-type electrodes for advanced pseudocapacitors

Journal:	*Journal of Materials Chemistry A*
Manuscript ID	TA-ART-01-2020-000697.R1
Article Type:	Paper
Date Submitted by the Author:	05-Mar-2020
Complete List of Authors:	Zhu, Yuanyuan; South China University of Technology Ji, Xu; Zhongkai University of Agriculture and Engineering, College of Automation Yang, Lufeng; Jinan university, Department of Chemistry Jia, Jin; South China University of Technology Cheng, Shuang; School of Environment and Energy, Center for New Energy Chen, Hailong; Georgia Institute of Technology, School of Mechanical Engineering Wu, Zhong-Shuai; Dalian Institute of Chemical Physics, Chinese Academy of Sciences, Dalian National Laboratory For Clean Energy Passarello, Donata; SLAC National Accelerator Laboratory Liu, Meilin; Georgia Institute of Technology, School of Materials Science and Engineering

Targeted synthesis and reaction mechanism discussion of Mo_2C based insertion-type electrodes for advanced pseudocapacitors

Yuanyuan Zhu†[a, e], Xu Ji†[b], Lufeng Yang[c], Jin Jia[d], Shuang Cheng[a,*], Hailong Chen[c], Zhong-Shuai Wu[e], Donata Passarello[f] and Meilin Liu[g]

[a] New Energy Research Institute, School of Environment and Energy, South China University of Technology, Guangzhou, 510006, People's Republic of China.

[b] College of Automation, Zhongkai University of Agriculture and Engineering, Guangzhou, 510225, People's Republic of China

[c] The Woodruff School of Mechanical Engineering, Georgia Institute of Technology, 771 Ferst Drive, Atlanta, GA 30332-0245, USA.

[d] Institute for Advanced Interdisciplinary Research, Collaborative Innovation Center of Technology and Equipment for Biological Diagnosis and Therapy in Universities of Shandong, University of Jinan, Jinan 250011, People's Republic of China.

[e] Dalian National Laboratory for Clean Energy, Dalian Institute of Chemical Physics, Chinese Academy of Sciences, 457 Zhongshan Road, Dalian 116023, People's Republic of China.

[f] Stanford Synchrotron Radiation Lightsource, SLAC National Accelerator Laboratory, Menlo Park, CA, USA

[g] School of Materials Science and Engineering, Georgia Institute of Technology, Atlanta, GA 30332-0245, USA.

† Yuanyuan Zhu and Xu Ji contributed equally to this work.

* Corresponding author. E-mail address: escheng@scut.edu.cn (S. Cheng).

Abstract: Mo_2C is one of the few compounds that possess good electronic conductivity. Meanwhile, it possesses nature 1D zigzag tunnel structure that is ideally suited for fast ion diffusion. Here, an effective approach is demonstrated for fabrication of structurally stable N-doped Mo_2C/C nanobelts. It demonstrates high and fast energy storage ability with initial capacitances of 1,139 C g^{-1} at 1 mV s^{-1}, 151 C g^{-1} at an extremely high scan rate of 2,000 mV s^{-1} and 208 C g^{-1} at a discharge current density of 200 A g^{-1}. After electrochemical activation of cycling, the capacity is continuously enhanced and much higher capacitances of 2,523 C g^{-1} at 1 mV s^{-1} and 1,403 C g^{-1} at 50 A g^{-1} are achieved after 15,000 cycles' cycling at 50 mV s^{-1}. Using power law, surface-controlled capacitive process is evaluated and it is over 90% when the scan rates are higher than 10 mV s^{-1} and still high as 73% at 1 mV s^{-1}. From *in-situ* synchrotron XRD, it is found that there is negligible crystal structure and volume change during charging/discharging, reflecting an insertion-type charge storage mechanism.

Keywords: Molybdenum carbide; Insertion-type pseudocapacitors; Carbon coating; *In-situ* synchrotron XRD

1. Introduction

Electrochemical capacitors with higher energy storage ability than conventional capacitors and better rate capacity and cycling life than batteries are becoming more and more attractive in many emerging fields,[1-3] such as electrical vehicles, portable electronics and smart grids for efficient and stable electrical energy storage. Electrical double-layer capacitors (EDLCs), as one of the two typical electrochemical capacitors,[4,

[5] store charge through physical adsorption/desorption mechanism and hence exhibit high rate capacity and durability but low energy density.[6, 7] Pseudocapacitors, in which much more charge can be stored *via* Faradic reaction, are expected to store more energy than EDLCs.[8] Though various transition metal-based compounds have been explored as pseudocapacitive electrodes, they generally show unsatisfied capacity, rate performance and cycling stability owning to the poor electronic/ionic conductivity and large volume change during cycling. To realize fast and high energy storage together with high durability, new potential candidates with optimized structure and good electronic conductivity need to be developed.

Transition metal carbides (TMCs) are just one type of promising candidates, which usually originate from the introduction of carbon atoms into the metal lattice and emerge novel and distinctive physical and chemical properties, including metallic conductivity and excellent corrosion resistance.[9-13] TMCs have been widely used in catalysis, electronic and other fields.[14-16] Since Gogotsi et al.[17] reported the electrochemical behavior of exfoliated Ti_2C as anode for lithium-ion battery in 2012, a series of carbides have been synthesized and used for lithium storage, such as Ti_3C_2,[18, 19] Nb_2C,[20] V_2C,[21] Cr_2C[22] and Mo_2C[23]. Among them, Mo_2C, with good electric conductivity (~1.02×10^2 S cm^{-1})[24, 25] and nature one-dimension (1D) tunnels that can serve as fast ion diffusion path, is one of the most promising electrodes to balance the capacity and the rate performance. However, there are rarely Mo_2C concerned reports as electrodes,[13, 23] which should own to its relative low theoretical capacity, only 473 C g^{-1} (~131 mAh g^{-1}) when considering one electron' transfer and 1,892 C g^{-1} (~524 mAh

g^{-1}) for four electrons' transfer where fully phase conversion of Mo_2C to Mo are predicted. Additionally, the synthesis of Mo_2C generally requires high-temperature calcination which would result in large bulks. Therefore, controlled-synthesis to realize the formation of nano-structured Mo_2C and the achievement of good charge storage performance are urgently needed.

Herein, a mild approach to prepare N-doped carbon coated Mo_2C (N-Mo_2C/C) nanobelts is proposed. Molybdenum source, MoO_3, pre-packaged with polypyrrole (PPY) is used as precursor. The N-Mo_2C/C delivers high initial capacities of 1,139 C g^{-1} at 1 mV s^{-1}, 151 C g^{-1} even at an extremely high scan rate of 2,000 mV s^{-1}, and 208 C g^{-1} at a discharge current density of 200 A g^{-1}, exhibiting high capacity and excellent rate performance. More importantly, there is no capacity fading but contentious increase over cycling test. After 15,000 cycles running at 50 mV s^{-1}, significantly elevated capacities of 2,523 C g^{-1} at 1 mV s^{-1}, 2,950 C g^{-1} at 0.5 A g^{-1} and 1,403 C g^{-1} at 50 A g^{-1} are achieved. Using the power law, it is found that the energy storage is dominated by the surface-controlled capacitive process. Using *in-situ* synchrotron XRD, the structural change during charging/discharging is explored. It is found that there is no phase change but slight expansion/contraction, implying insertion-type charge storage process along the 1D tunnels.

2. Experimental

2.1 Materials and Chemicals

Molybdenum powder (99.9%) is purchased from Aladdin Chemistry Co. Ltd (Shanghai,

China). Hydrogen peroxide aqueous solution (H_2O_2, 30%) and ammonium persulfate are supplied by Damao chemical reagent factory (Tianjin, China). Pyrrole comes from Macklin Biochemical Co. Ltd (Shanghai, China). All the chemicals were used as received without further purification. Deionized water with resistivity of 18.2 MΩ cm^{-1} is prepared using a Millipore purification system (Milli-Q®).

2.2 Preparation of the N-doped Mo_2C/C composites

Firstly, MoO_3 nanobelts are synthesized according to the following procedure: 1.0 g molybdenum (Mo) powder is added into 10 mL H_2O_2 (30%) solution and kept in an ice bath under stirring until a yellow solution is formed; then, 20 mL deionized water is added into the solution followed by continuous stirring for 30 min before transferred into a 50 mL Teflon-lined stainless-steel autoclave for hydrothermal treatment at 200 °C for 24 h; after cooling to room temperature, white precipitate of MoO_3 is collected through vacuum filtration, washing with deionized water and drying at 70 °C for 12 h. Secondly, MoO_3@ppy is obtained according to the following procedure: 0.1 g of the as-prepared MoO_3 is dispersed into 100 mL ammonium persulfate (7.5 mM) before 0.1 g pyrrole monomers is added in for polymerization; the above solution is kept in an ice bath for 12 h under stirring; black precipitate of MoO_3@ppy is collected after vacuum filtration, washing and drying. Finally, the target sample of N-Mo_2C/C powder is harvested through controlled calcinations at 700 °C for 4 h in N_2 flowing.

2.3 Materials characterization

Phase compositions and crystal structure of the products were determined by X-ray diffraction (XRD) on a D8 Advance (Germany Bruker) X-ray diffractometer using Cu

Kα radiation (λ = 0.15406 nm) at 40 kV and 40 mA. Morphologies of the products were observed by field emission scanning electron microscopy (FE-SEM, Hitachi SU8010) and transmission electron microscopy (TEM, JEM-2100F Field Emission Electron Microscope, Japan). X-ray photoelectron spectroscopic (XPS) was operated on a PHI X-tool instrument (Ulvac-Phi). Raman spectra were recorded by a LabRAM HR800 spectrometer (Horiba Jobin Yvon, France) equipped with a semiconductor laser (wavelength = 532 nm). Brunauer-Emmet-Teller (BET) surface area was determined using a micromeritics ASAP 2020 analyzer with nitrogen adsorption at 77 K. Thermal Gravimetric Analysis (TGA) was performed using a Mettler-Toledo TGA/DSC1 apparatus between 30 °C and 700 °C at a ramping rate of 10 °C min^{-1} under air flowing.

Temperature-dependent *in-situ* XRD patterns were collected using the same diffractometer mentioned above equipped with an Anton Paar XRK 900 high-temperature reaction chamber. The sample was heated from 30 °C to 700 °C with a heating rate of 5 °C min^{-1} under N_2 flow with a space velocity of 30 mL min^{-1}. Before each XRD pattern was collected, the sample was hold at setting temperature for 30 min. All the diffraction patterns were recorded in the range of 10 ~ 80° with a step size of 0.02° and a scanning rate of 0.08° s^{-1}.

In-situ synchrotron X-ray diffraction (SXRD) was performed using a synchrotron radiation source (λ = 0.8856 Å) with beamline 7-2 in transmission mode, at Stanford Synchrotron Radiation Light source (SSRL), SLAC National Accelerator Laboratory Menlo Park, CA, USA. The patterns were collected every 2 min. The *in-situ* test began with discharging from open circuit voltage and then charging in the range of 0.01 ~ 3

V (vs. Li/Li^+) at a current density of 0.2 A g^{-1} towards the half-cell with lithium foil as counter electrode.

2.4 Electrochemical measurements

Typically, working electrodes were prepared by mixing 80 wt% active materials, 10 wt% acetylene black, and 10 wt% polyvinylidene difluorides in N-Methyl pyrrolidone (NMP) solvent. The slurry was coated on copper foil and dried before sealed in a CR2032 coin cell as an electrode using 1 M $LiClO_4$ in propylene carbonate, ethylene carbonate and dimethyl carbonate solution (PC: EC: DMC, 1: 1: 1 in volume ratio) with 5% fluoroethylene carbonate as electrolyte and lithium wafer as counter electrode, a typical half-cell. The assembly process was carried out in an argon-filled glove box with concentrations of moisture and oxygen below 0.1 ppm. The electrochemical performances were characterized by cyclic voltammetry (CV) and galvanostatic charge-discharge (GCD) techniques within a potential window of 0.01 ~ 3 V (vs. Li/Li^+) using a CHI 660E electrochemical workstation. Electrochemical impedance spectra (EIS) were measured using a Solartron 1260 Impedance Analyzer in a frequency range of 0.1 Hz to 100 KHz with perturbation voltage of 10 mV at open-circuit potential.

3. Results and discussion

To take control of the phase change during calcination and optimize the target crystal structure, *in-situ* XRD measurement was employed to the MoO_3@ppy precursor and a series of XRD patterns were collected along the temperature rising from 30 to 700 °C in N_2 flow, as presented in **Fig. 1f**. There is no phase change when the temperature is lower than 200 °C; while, PPY begin to be carbonized accompanied by the

pulverization of MoO_3 at 300 °C; then the MoO_3 is completely reduced to be MoO_2 when the temperature is up to 400 °C; the MoO_2 phase is maintained in a relative wide temperature range before it is carbonized to be Mo_2C at 700 °C. Phase transition of the MoO_3@ppy can be expressed accordingly[24]:

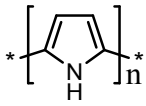

$$\rightarrow C + CH_x \uparrow \quad (1)$$

$$MoO_3 + C \rightarrow MoO_2 + CO_x \quad (2)$$

$$MoO_2 + C \rightarrow Mo_2C + CO_x \quad (3)$$

Morphology change of the sample at different stage is characterized by SEM. The firstly synthesized MoO_3 is composed of nanobelts in a large-area with width of around 200 ~ 300 nm and relatively smooth surface, as shown in **Fig. 1a**. The following polymerization of PPY on the surface (MoO_3@ppy) does not change the morphology of the nanobelts (**Fig. 1h**). After subsequent calcination for the preparation of Mo_2C, the nanobelt structure is well kept and abundant nanoparticles were formed on surface (**Fig. 1g**). A brief schematic of the formation procedure is accordingly drafted in **Fig. 1b**.

The structure of the Mo_2C is further investigated using TEM in **Fig. 1c**. It is found the whole nanobelt is composed of small particles with a thin and uneven coating layer. Not only the surface but also the bulk of the nanobelt is porous. In an enlarged HRTEM view of **Fig. 1d**, apparent lattice fringe spaces of 0.228 and 0.236 nm that come from different crystal particles and correspond to the (211) and (020) planes of Mo_2C respectively are observed, confirming the phase composition of the nanoparticles. The surface coating layer with a thickness of several nanometers is defined to be C with a

relatively large lattice space of 0.383 nm that is indexed to the typical (002) plane, implying the successful coating of C on the surface. Mass proportion of the C in the Mo_2C/C composite is around 9 wt % based on TGA result (**Fig. S1**†). From selected area electron diffraction (SAED) pattern (**Fig. 1e**), bright diffraction rings can be observed, which are attributed to the (002), (020), (221), (203) and (231) planes of Mo_2C, indicating a polycrystalline structure. Element mapping images (**Fig. 1j-l**) of one nanobelt (**Fig. 1i**) demonstrate that there are not only Mo and C elements but also evident N, indicating the doping of N. According to the above analysis, it can be concluded that during the pyrolysis process, N-Mo_2C/C, is formed through carbonization and reduction accompanied by N doping, in where PPY works as N source for doping and C source for the carbonization of MoO_3 to form Mo_2C and excess C is left on the surface as coating layers.

Phase compositions and structural information of the final product were further determined by XRD patterns and Raman spectra in **Fig. 2a-b**. XRD pattern of the white precipitation (blue curve of **Fig. 2a**) collected from the hydrothermal product matches well with the orthorhombic MoO_3 phase (JCPDS no. 89-5108), confirming the formation of high purity and well-crystallized MoO_3. After pyrolysis, diffraction peaks located at 34.64, 38.02, 39.67, 52.23, 61.66, 69.58, and 74.83 º in the red curve of **Fig. 2a** can be respectively ascribed to the (002), (020), (211), (221), (203), (231), and (223) planes of orthorhombic Mo_2C with a space group of Pca21 (JCPDS no. 77-0720). There are no other additional peaks, indicating the fully conversion of MoO_3 to Mo_2C. Raman spectra were also captured for the MoO_3 and the N-Mo_2C/C in **Fig. 2b**. All the

detectable Raman bands centered at 995, 818, 666, 378, 338, 291, 245, 159 and 128 cm^{-1} can be indexed to the orthorhombic MoO_3 (the blue curve). Characteristic D and G bands assigned to carbon can be detected and no Raman active vibrations indexed to Mo_2C can be observed for the N-Mo_2C/C, which coincides with the other Mo_2C concerned reports.[26-28]

To gain detailed information for the N-doping, surface chemical composition of the N-Mo_2C/C was further explored by XPS and fitted with Gaussian Law in **Fig. 2d-f**. Five peaks centered at around 232.08 eV, 284.08 eV, 398.08 eV, 416.08 eV and 530.08 eV that can be ascribed to Mo 3d, C 1s, N 1s, Mo 3p and O 1s respectively are distinguished from the survey spectrum (**Fig. S2†**). The high-resolution Mo 3d XPS spectrum (**Fig. 2d**) can be divided into six peaks, ascribable to Mo^{2+} (228.7 and 232.1 eV), Mo^{4+} (229.5 and 232.8 eV) and Mo^{6+} (232.6 and 235.9 eV) species,[29-31] respectively, implying partial surface oxidation of the Mo_2C.[14, 30, 31] In the high-resolution C 1s spectrum (**Fig. 2e**), a characteristic peak of Mo-C bond in Mo_2C at 284.5 eV, and four more peaks at 285.0 eV, 285.8 eV, 287.0 eV and 288.9 eV that correspond to Csp^2-Csp^2, N-Csp^2, N-Csp^3 and O-C=O bonds respectively can be fitted, indicating that some of the N are successfully doped into the C matrix,[30, 32] which is helpful for the electron transport. The high-resolution N 1s spectrum (**Fig. 2f**) was deconvoluted into four peaks: the peaks at 396.98, 398.7 and 400.1 eV can be assigned to pyridinic-N, pyrrolic-N and graphitic-N, respectively; the peak at 394.9 eV corresponds to Mo-N bond,[23, 30, 32-34] indicating that there is also N-doping in the Mo_2C matrix. The Mo-N bond formed between the Mo_2C and the C coating layer is expected

to maintain their well contact during reiterative charging/discharging, which is beneficial to the stability.[30, 32, 35]

Moreover, specific surface areas of the MoO_3 and the N-Mo_2C/C were also collected using N_2 sorption and desorption isotherms (**Fig. 2c**), which are calculated to be 7.95 and 36.34 m^2g^{-1} respectively with the Brunauer-Emmett-Teller (BET) theory. The higher specific surface area of the N-Mo_2C/C nanobelts than that of the MoO_3 nanobelts reflects that extra pores are formed during the carbonization process, consisting with the SEM results. Detailed pore size distributions for the MoO_3 (blue) and the N-Mo_2C/C (red) are presented in the illustration of **Fig. 2c**. There are more pores for the N-Mo_2C/C, which will facilitate the ion diffusion and will ease volume expansion during charging/discharging.

To evaluate the charge storage ability of the porous N-Mo_2C/C, CV and GCD measurements in a potential window of 0.01 to 3.0 V vs Li/Li^+ were performed in **Fig. 3**. In the CV curves (**Fig. 3a** and **b**), a very weak redox pair with a cathodic peak at around 1.2 V and an anodic peak at about 1.5 V can be observed, which is ignorable when the sweep rates are higher than 20 mV s^{-1}. The redox pair has been attributed to the conversion reaction of $Mo_2C + xLi^+ + xe^- \rightarrow 2Mo^0 + Li_xC$ in the previous reports,[12, 23, 36] but no evidence that supports this view has ever been provided. More work needs to be carried out to disclose the origin of this redox pair. Consistently, negligible charge and discharge platforms at around 1.5 V/1.2 V are observed in the near-linear GCD curves at different current densities from 0.5 to 200 A g^{-1} in **Fig. 3c** and **d**. Specific capacities calculated from the

CV and the GCD results are shown in **Fig. 3e**. A capacity of 1,139 C g^{-1} (316 mAh g^{-1}) can be achieved at a scan rate of 1 mV s^{-1} and still up to 151 C g^{-1} at an extremely high scan rate of 2,000 mV s^{-1}, which means considerable energy can be stored in less than 2 second. While, the capacity is up to 1,225 C g^{-1} at a current density of 0.5 A g^{-1} and a high capacity of 208 C g^{-1} is maintained at 200 A g^{-1}, indicating high capability and remarkable rate performance, much better than most Mo-based electrochemical electrodes (**Table S1**), especially in organic electrolytes.[37-39]

In addition, long-term cycling stability, another important parameter to evaluate the N-Mo_2C/C electrode is characterized at 50 mV s^{-1} in **Fig. 3g**. Surprisingly, there is no decay but obvious increase for the capacity along cycling, gradually rising in the first 5,000 cycles and then maintained in the following 10, 000 cycles with a final capacity as high as ~1,120 C g^{-1}. There is another thing worth mentioning that the Coulombic efficiency is close to 100% during the whole cycling test (blue curve in Fig. 3g). After cycling, the capacity can reach 2,523 C g^{-1} at 1 mV s^{-1} and 2,950 C g^{-1} at 0.5 A g^{-1}, and still be capable of up to 358 C g^{-1} at 200 A g^{-1} (see **Fig. S3**† and inset of **Fig. 3g**). The performance enhancement should be concerned with the impedance decline after cycling, as shown in the EIS of **Fig. 3f**.

To conduct more in-depth investigations, morphology and structure change of the electrode after cycling were also collected with SEM (**Fig. S4**†) and HRTEM (**Fig. S5**†). From the SEM image, it can be seen that the nanobelt structure is well maintained but a more porous surface (see zoom-in image of **Fig. S4b**†). From the HRTEM images

(**Fig. S5b†**), no obvious crystal particles or lattice fringes can be observed, implying that the well patterned crystal structure is destroyed and amorphous structure is formed after long-term cycling, which is consistent with the SAED (**Fig. S5c†**), no spots or circular arcs can be observed. Moreover, the shell seems to be thicker, close to ~20 nm after cycling (see **Fig. S5a†**), which is only several nanometers before cycling (see Fig. 1c). Therefore, there are three possible reasons for the capacity enhancement: the better wetting property of electrolyte owning to the more porous structure of the electrode, the improved diffusion and accommodation ability of electrolyte ions because of the disappearance of grain boundaries at the interface and the bulk (activity process of the material itself) and the possible formation of organic polymeric layer resulted from the decomposition of the electrolyte, which can deliver excess capacity.[40-44]

In order to gain insight information for the charge storage mechanism, the dependence of peak current (i) on sweep rate (v) is evaluated in **Fig. 4**. The plot of log (i) versus log (v) from 0.1 to 10 mV s^{-1} is displayed in **Fig. 4a** and the b value that reflects the contribution of capacitive process is calculated with the power law: $i = a\, v^b$, where a and b are alterable parameters.[19, 37, 45] It is well accepted that the current response is diffusion-controlled battery-type process when $b = 0.5$ while it is surface-controlled capacitive process when $b = 1$.[46] For the N-Mo_2C/C electrode, high b values of 0.91 and 0.9 are attained for the cathodic and anodic peaks respectively, implying that surface capacitive effect is predominant. In detail, it is a combination of two mechanisms, surface-controlled capacitive mechanism (k_1v) and diffusion-controlled mechanism ($k_2v^{1/2}$), expressed as: $i\ (V) = k_1v + k_2v^{1/2}$, where k_1 and k_2 are alterable

parameters.[46] By determining the values of k_1 and k_2, fraction of the current caused by capacitive contribution and battery-type contribution can be determined.

As shown in **Fig. 4c-f**, the gray areas represent the capacitive contribution at 1, 2, 5, and 10 mV s^{-1}. The ratio of capacitive contribution increases along with the sweep rate and is up to 90 % at 10 mV s^{-1}, as shown in **Fig. 4b**. Even when the sweep rate is low as 1 mV s^{-1}, the capacitive contribution is still up to ~73%, indicating that the charge storage process is predominantly surface limited and the charge diffusion in bulk is very fast, which should be the main reason for the high rate performance.

Structure evolution of the N-Mo_2C/C electrode during charging/discharging is investigated by *in-situ* SXRD measurement in **Fig. 5** and **S6†**. During this measurement, the half-cell was firstly discharged to 0.01 V from an open circuit potential (OCP) of around 2.6 V and then charged to 3 V. The result shows that no new Bragg peaks is seen except those indexed to Mo_2C. The peaks of Mo_2C remain almost intact during one cycle' charging/discharging, which are gradually weakening along long-term cycling. From the partial enlarged patterns in **Fig. S6†**, slight shifts of the (002), (211), and (203) peaks to lower angle during discharging can be observed, indicating a very slight expansion of the Mo_2C crystal. Opposite change can be observed during charging. The size of the zigzag 1D tunnel along the *z*-axis is rather large, as shown in **Fig. 5a**, the slight change of the crystal structure of Mo_2C implies that most of the charge is stored in the tunnels through fast diffusion and insertion-type capacity makes the main contribution, which agrees well with the above analysis to Fig. 4.

The initial capacitance of the N-Mo_2C/C electrode is higher than the theoretical value evaluated from one electron concerned insertion mechanism. After activation of long-term cycling, the capacitance is increased and is even higher than the theoretical value (1,892 C g^{-1}/524 mAh g^{-1}) calculated according to the well-accepted phase conversion mechanism (Mo_2C to Mo). While no LiC_6 or Mo phases is identified in the synchrotron XRD pattern even at fully discharged state (0.1 V). Massive formation of their amorphous phases can also be excluded by the negligible intensity change of the Mo_2C peaks in a whole charging/discharging cycle (see **Fig. 5b**). It can be concluded that most of the charges are stored in the 1D tunnel, while the detailed occupying mode needs further investigation.

4. Conclusion

In this work, a co-step of doping and carbonization is developed to fabricate structurally stable N-doped Mo_2C/C for ultrafast and high-energy storage. Benefited from the nature properties of Mo_2C (good electronic conductive and nature tunnel structure suited for fast ionic diffusion) and the well-designed structure of the composite, the electrodes exhibit fast and high energy storage ability. High initial capacities of 1,139 C g^{-1} at 1 mV s^{-1}, 151 C g^{-1} at extremely high scan rate of 2,000 mV s^{-1} and 208 C g^{-1} at 200 A g^{-1} are achieved. After 15,000 cycles' long-term cycling, the capacitances are improved to be 2,523 C g^{-1} at 0.5 A g^{-1} and 1,403 C g^{-1} at 50 A g^{-1}. Charge storage mechanism of the electrode is evaluated with the power law and *in-situ* synchrotron XRD measurements. It is found that surface-controlled capacitive process makes the

main contribution to the capacity, over 90 % when the sweep rate is higher than 10 mV s^{-1} and still high as 73% at 1 mV s^{-1}. There is no phase change but very slight and reversible crystal expansion/contraction during discharging/charging, implying that most of the charges are stored in the 1D tunnels, a typical feature of insertion-type pseudocapacitive electrode. The good electrochemical performance of the Mo_2C/C composite exhibits here makes it promising candidate to achieve high power and energy density simultaneously.

Conflicts of interest

There are no conflicts to declare.

Acknowledgements

This work was supported by the Fundamental Research Funds for Central Universities of SCUT, China (no. 2018ZD20), National Science Foundation of Guangdong Province, China (no. 2020A1515010485), the National Science Foundation for Key Support Major Research project of China (No. 91745203). The authors also want to acknowledge Dr. Bart A. Johnson for his help in synchrotron data collection. Use of the Stanford Synchrotron Radiation Light source, SLAC National Accelerator Laboratory, is supported by the U.S. Department of Energy, Office of Science, and Office of Basic Energy Sciences under Contract No. DE-AC02-76SF00515.

References

1. M. Winter and R. J. Brodd, *Chem. Rev.*, 2004, **104**, 4245-4269.

2. J. R. Miller and P. Simon, *Science*, 2008, **321**, 651-652.

3. L. Yuting, H. Rong, F. Yongzheng, Z. Kai, C. Kui, Y. Jun, Y. Ke, W. Guiling and C. Dianxue, *Nano-Micro Lett.*, 2019, **11**, 30.

4. P. Simon and Y. Gogotsi, *Nature Mater.*, 2008, **7**, 845-854.

5. P. Zhibin, H. Haibo, L. Guojin and Y. Changhui, *Nano-Micro Lett.*, 2017, **9**, 19.

6. L. L. Zhang and X. S. Zhao, *Chem. Soc. Rev.*, 2009, **38**, 2520-2531.

7. J. Li, X. Yun, Z. Hu, L. Xi, N. Li, H. Tang, P. Lu and Y. Zhu, *J. Mater. Chem. A*, 2019, **7**, 26311-26325.

8. G. Wang, L. Zhang and J. Zhang, *Chem. Soc. Rev.*, 2012, **41**, 797-828.

9. H. H. Hwu and J. G. Chen, *Chem. Rev.*, 2005, **105**, 185-212.

10. J. A. Nelson and M. J. Wagner, *Chem. Mater.*, 2002, **14**, 1639–1642.

11. X.-R. Shi, J. Wang and K. Hermann, *J. Phys. Chem. C*, 2010, **114**, 13630-13641.

12. Y. Xiao, L. Zheng and M. Cao, *Nano Energy*, 2015, **12**, 152-160.

13. Q. Sun, Y. Dai, Y. Ma, T. Jing, W. Wei and B. Huang, *J. Phys. Chem. Lett.*, 2016, **7**, 937-943.

14. C. Wan, Y. N. Regmi and B. M. Leonard, *Angew. Chem. Int. Ed.*, 2014, **53**, 6407-6410.

15. S. B. Yin, M. Cai, C. X. Wang and P. K. Shen, *Energy Environ. Sci.*, 2011, **4**, 558-563.

16. Z. X. Yan, H. E. Wang, M. P. Zhang, Z. F. Jiang, T. S. Jiang and J. M. Xie, *Electrochim. Acta*, 2013, **95**, 218-224.

17. M. Naguib, J. Come, B. Dyatkin, V. Presser, P. L. Taberna, P. Simon, M. W. Barsoum and Y. Gogotsi, *Electrochem. Commun.*, 2012, **16**, 61-64.

18. Z. F. Lin, D. Barbara, P. L. Taberna, K. L. Van Aken, B. Anasori, Y. Gogotsi and P. Simon, *J. Power Sources*, 2016, **326**, 575-579.

19. J. Yan, C. E. Ren, K. Maleski, C. B. Hatter, B. Anasori, P. Urbankowski, A. Sarycheva and Y. Gogotsi, *Adv. Funct. Mater.*, 2017, **27**, 1701264.

20. O. Mashtalir, M. R. Lukatskaya, M. Q. Zhao, M. W. Barsoum and Y. Gogotsi, *Adv. Mater.*, 2015, **27**, 3501-3506.

21. M. Naguib, J. Halim, J. Lu, K. M. Cook, L. Hultman, Y. Gogotsi and M. W. Barsoum, *J. Am. Chem. Soc.*, 2013, **135**, 15966-15969.

22. Z. Xu, X. Lv, J. Chen, L. Jiang, Y. Lai and J. Li, *Phys. Chem. Chem. Phys.*, 2017, **19**, 7807-7819.

23. Q. Gao, X. Zhao, Y. Xiao, D. Zhao and M. Cao, *Nanoscale*, 2014, **6**, 6151-6157.

24. W. Tian, H. Hu, Y. Wang, P. Li, J. Liu, J. Liu, X. Wang, X. Xu, Z. Li, Q. Zhao, H. Ning, W. Wu and M. Wu, *ACS Nano*, 2018, **12**, 1990-2000.

25. S. L. F. L. D. W. C. H. Y. Z. J. B. B. J. Xu, *Small Methods*, 2018, **2**, 1800040.

26. M. Li, Y. Zhu, H. Wang, C. Wang, N. Pinna and X. Lu, *Adv. Energy Mater.*, 2019, **9**, 1803185.

27. D. Hou, J. Zhang, Q. Li, P. Zhang, C. Chen, D. Yan and Y. Mai, *Langmuir*, 2018, **34**, 10924-10931.

28. J. Zhu, Y. Yao, Z. Chen, A. Zhang, M. Zhou, J. Guo, W. D. Wu, X. D. Chen, Y. Li and Z. Wu, *ACS Appl. Mater. Interfaces*, 2018, **10**, 18761-18770.

29. Y. Zhao, K. Kamiya, K. Hashimoto and S. Nakanishi, *J. Am. Chem. Soc.*, 2015, **137**, 110-113.

30. R. Ma, Y. Zhou, Y. Chen, P. Li, Q. Liu and J. Wang, *Angew. Chem. Int. Ed.*, 2015, **54**, 14723-14727.

31. H. Lin, Z. Shi, S. He, X. Yu, S. Wang, Q. Gao and Y. Tang, *Chem. Sci.*, 2016, **7**, 3399-3405.

32. Y. Lu, H. Ang, Q. Yan and E. Fong, *Chem. Mater.*, 2016, **28**, 5743-5752.

33. J. T. Ren, L. Chen, C. C. Weng, G. G. Yuan and Z. Y. Yuan, *ACS Appl. Mater. Interfaces*, 2018, **10**, 33276-33286.

34. C. Lu, D. Tranca, J. Zhang, F. N. Rodri Guez Hernandez, Y. Su, X. Zhuang, F. Zhang, G. Seifert and X. Feng, *ACS Nano*, 2017, **11**, 3933-3942.

35. R. Li, S. Wang, W. Wang and M. Cao, *Phys. Chem. Chem. Phys.*, 2015, **17**, 24803-24809.

36. J. Zhu, K. Sakaushi, G. Clavel, M. Shalom, M. Antonietti and T. P. Fellinger, *J. Am. Chem. Soc.*, 2015, **137**, 5480-5485.

37. H. S. Kim, J. B. Cook, H. Lin, J. S. Ko, S. H. Tolbert, V. Ozolins and B. Dunn, *Nat. Mater.*, 2017, **16**, 454-460.

38. G. Zhang, T. Xiong, M. Yan, L. He, X. Liao, C. He, C. Yin, H. Zhang and L. Mai, *Nano Energy*, 2018, **49**, 555-563.

39. B. Yu, D. Yang, Y. Hu, J. He, Y. Chen and W. He, *Small Methods*, 2019, **3**, 1800287.

40. H. Wu, G. Yu, L. Pan, N. Liu, M. T. McDowell, Z. Bao and Y. Cui, *Nat. Commun.*, 2013, **4**, 1943.

41. Y. Sun, X. Hu, W. Luo, F. Xia and Y. Huang, *Adv. Funct. Mater.*, 2013, **23**,

2436-2444.

42. X. Wu, Z. Wang, M. Yu, L. Xiu and J. Qiu, *Adv. Mater.*, 2017, **29**, 1607017.

43. L. Wang, Q. Zhang, J. Zhu, X. Duan, Z. Xu, Y. Liu, H. Yang and B. Lu, *Energy Storage Mater.*, 2019, **16**, 37-45.

44. Q. Zhang, L. Wang, J. Wang, X. Yu, J. Ge, H. Zhang and B. Lu, *J. Mater. Chem. A*, 2018, **6**, 9411-9419.

45. H. Lindstrom, S. Sodergren, A. Solbrand, H. Rensmo, J. Hjelm, A. Hagfeldt and S. E. Lindquist, *J. Phys. Chem. B*, 1997, **101**, 7717-7722.

46. J. Wang, J. Polleux, J. Lim and B. Dunn, *J. Phys. Chem. C*, 2007, **111**, 14925-14931.

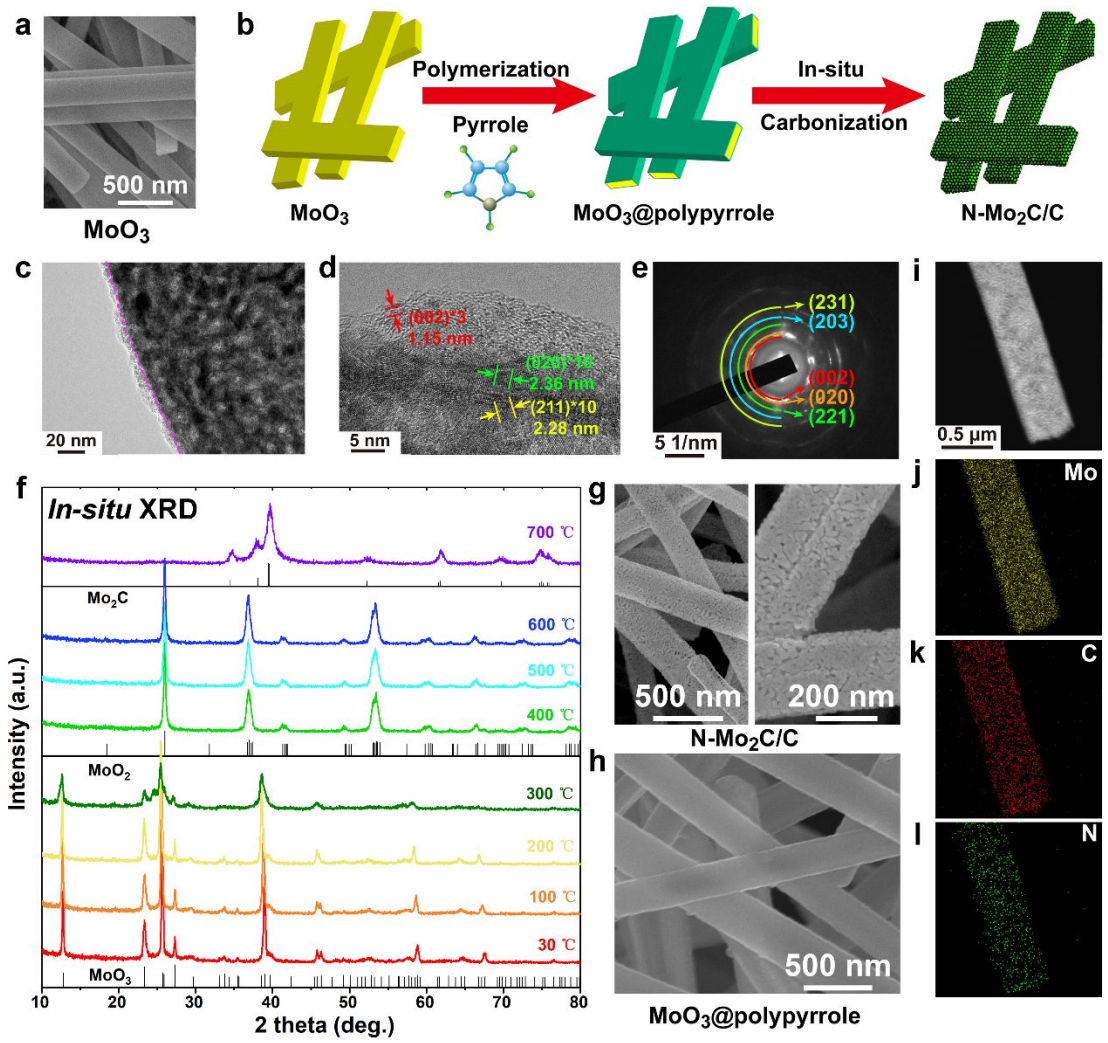

Fig. 1 (a) SEM image of the MoO_3; (b) schematic illustration for the formation process of the N-Doped Mo_2C/C nanobelts; (c) TEM, (d) HRTEM and (e) SAED images of the N-Mo_2C/C nanobelts; (f) *In-situ* XRD patterns, reflecting the phase change of the MoO_3@ppy powder along calcinations from 30 to 700 °C in a flowing nitrogen atmosphere; SEM images of (g) the N-Mo_2C/C and (h) the MoO_3@ppy; (i-l) STEM image and the corresponding Mo, C, and N elemental mappings of the N-Mo_2C/C.

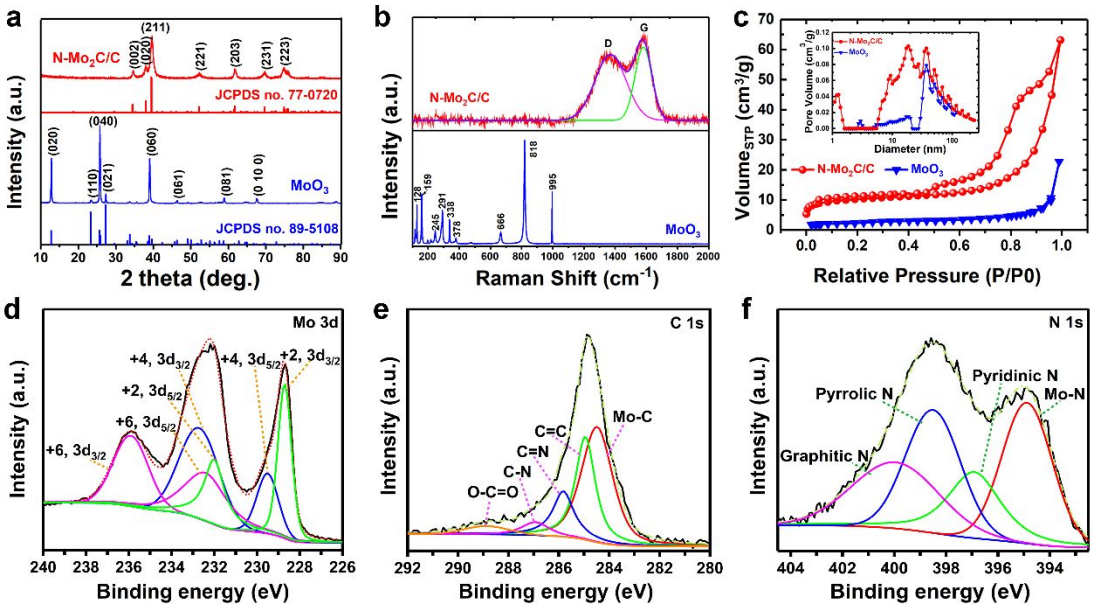

Fig. 2 (a) XRD patterns, (b) Raman spectra and (c) N_2 adsorption and desorption isotherms, inset is pore size distributions of the MoO_3 (blue) and the N-Mo_2C/C (red); XPS spectra of (d) Mo 3d, (e) C 1s and (f) N 1s of the N-Mo_2C/C.

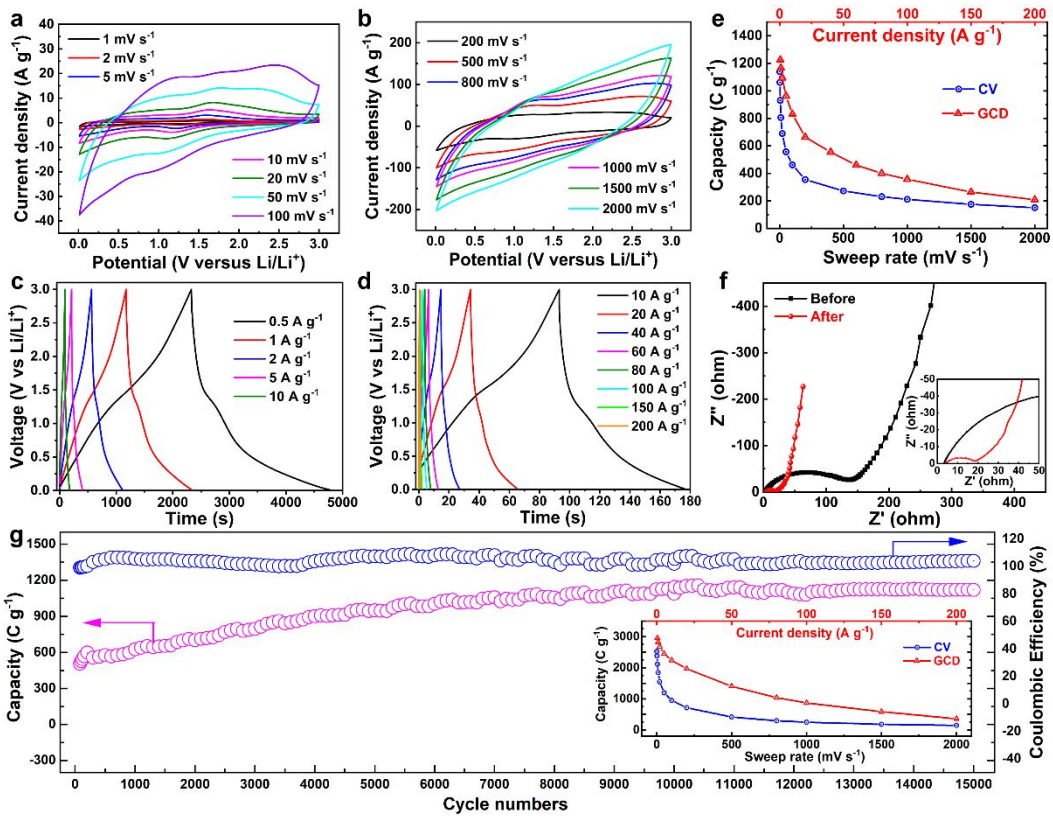

Fig. 3 Electrochemical performance of the N-Mo_2C/C nanobelts: (a) and (b) CV curves obtained at different scan rates from 1 to 2000 mV s^{-1} with a potential window ranging from 0.01 to 3 V (vs Li/Li^+); (c) and (d) GCD curves tested at different current densities from 0.5 to 200 A g^{-1}; (e) gravimetric capacity plots calculated based on the CV (blue curve) and the GCD (red curve) results; (f) Nyquist plots before and after long-term cycling; (g) long-term cycling behavior measured at 50 mV s^{-1}, inset is the gravimetric capacity plots after cycling.

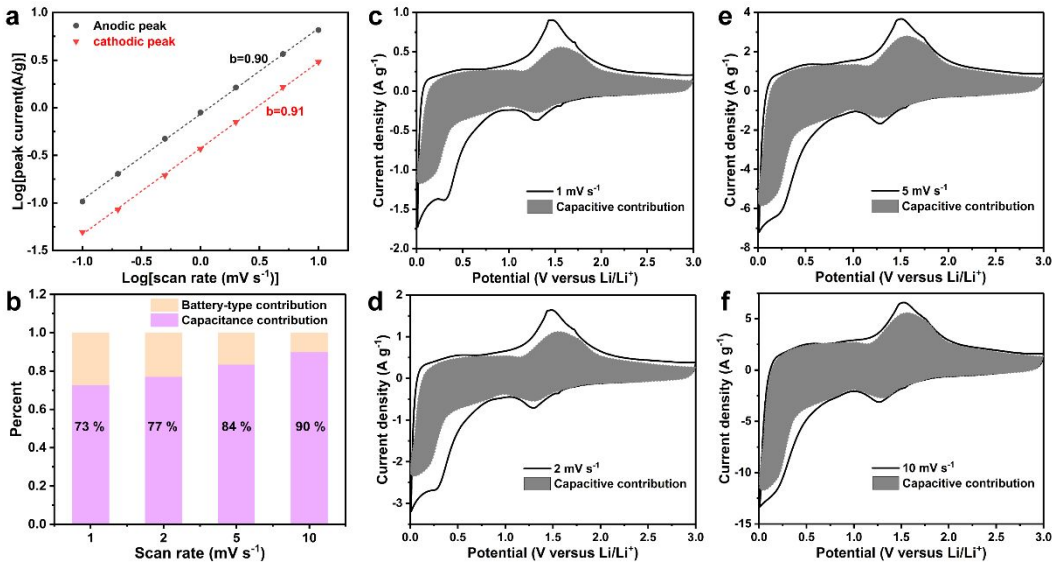

Fig. 4 (a) Plots of anodic (black curve) and cathodic (red curve) peak current against scan rate from 0.1 to 10 mV s^{-1} for the N-Mo_2C/C, slopes of these lines reflect *b* values; (b) Surface-controlled capacitive contribution to the capacity at different scan rates; Capacitive contribution represented by gray areas at different scan rates of (c) 1 mV s^{-1}, (d) 2 mV s^{-1}, (e) 5 mV s^{-1} and (f) 10 mV s^{-1}.

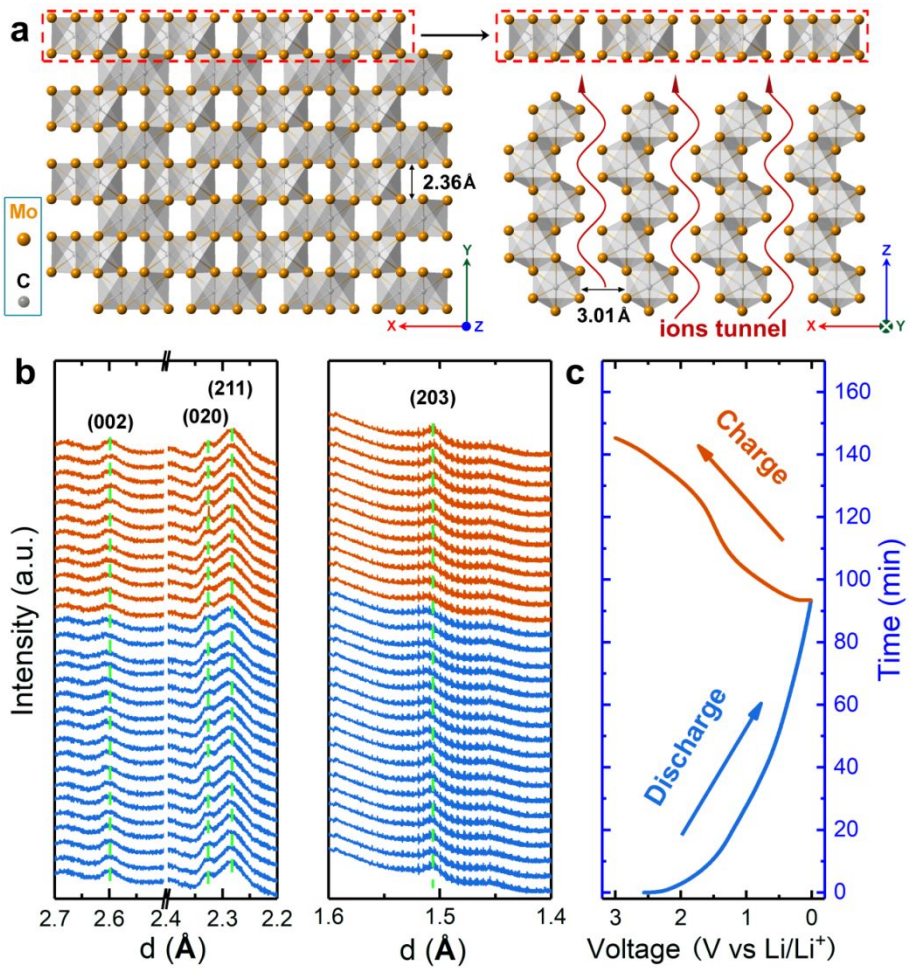

Fig. 5 (a) Typical crystal structure of the Mo_2C viewed from different directions; (b) *In-situ* SXRD patterns of the N-Mo_2C/C electrode in selected d-spacing ranges, highlighting the evolution of the (002), (020), (211) and (203) peaks of Mo_2C; (c) Charging/discharging curve collected during *in-situ* test.